

# Synchronizing Bloch-oscillating free carriers in moiré flat bands

Ali Fahimniya<sup>1</sup>, Zhiyu Dong<sup>1</sup>, Egor I. Kiselev<sup>2</sup>, Leonid Levitov<sup>1</sup>

<sup>11</sup>*Physics Department, Massachusetts Institute of Technology, Cambridge, Massachusetts 02139, USA*

<sup>2</sup>*Institut für Theorie der Kondensierten Materie,  
Karlsruher Institut für Technologie, 76131 Karlsruhe, Germany*

Achieving Bloch oscillations of free carriers under a direct current, a long-sought-after collective many-body behavior, has been notoriously hard due to stringent constraints on the band properties. We argue that the flat bands in moiré graphene fulfill the basic requirements for observing Bloch oscillations, offering an appealing alternative to the stacked quantum wells used in previous work aiming to achieve this regime. Bloch-oscillating moiré superlattices emit a comb-like spectrum of incommensurate frequencies, a property of interest for converting direct currents into high-frequency currents and developing broad-band amplifiers in THz domain. The oscillations can be synchronized through coupling to an oscillator mode in a photonic or plasmonic resonator. Phase-coherent collective oscillations in the resonant regime provide a realization of current-pumped THz lasing.

Bloch oscillations, arising when electrons are driven through a perfect crystal lattice by an electric field, are an iconic example of a coherent dynamics in quantum many-body systems[1, 2]. The oscillations are at the same frequency for all carriers, for a one-dimensional lattice given by  $\omega = eEa/\hbar$  with  $E$  the field strength and  $a$  the lattice period. Besides the obvious fundamental appeal, this behavior has long been eyed as a promising way to convert direct currents into high-frequency currents[3]. Wide interest in this phenomenon stems from the expectation that Bloch-oscillating electrons have the potential to provide broad band gain at THz frequencies[4, 5] and become the basis of a technology that will help fill the “THz gap”, leading to radiation emitters and detectors operating in this frequency range[6].

While Bloch oscillations have long been immortalized in textbooks, realizing them in solids has proven to be a challenging task. Achieving this regime requires overcoming several obstacles. One is the dephasing due to electron energy loss to phonons. To suppress phonon emission exceptionally narrow electronic bands of width smaller than the optical phonon energy must be used. Another is the dephasing due to disorder scattering. Experimental efforts so far mainly focused on synthetic MBE-grown semiconductor superlattices, which host narrow minibands tunable by the superlattice design parameters[6–9]. These systems cleared a number of key milestones on the road towards achieving Bloch oscillations. Namely, they display the signatures indicative of Bloch oscillations, such as negative differential conductivity  $dI/dV < 0$ , recurrence and ringing in the optical pump-probe measurements, Wannier-Stark ladders and, last but not least, optical gain[6–9]. However, upon the injection current approaching the relevant parameter range the superlattice systems develop instabilities and show a complex noisy behavior due to the onset of switching and formation of electric domains. This behavior presents the main obstacle to achieving the collective globally-synchronized Bloch oscillations[11–13].

Meanwhile, recently Bloch oscillations were achieved in cold atom systems, using Bloch minibands in optical lattices[14–18]. Because the systems is charge-neutral,

instead of the electric field the force of gravity had to be used to accelerate particles. This proof-of-principle demonstration has greatly improved our understanding of the underlying physics[19, 22] and strengthened interest in demonstrating electronic Bloch oscillations.

Given the difficulties encountered in semiconducting superlattices it is natural to seek other systems that meet the requirements for achieving Bloch oscillations, but are not prone to the electric domain formation instabilities. One enticing opportunity is offered by the recently introduced moiré superlattices in twisted bilayer graphene, a material that hosts electron bands that are tunable by the twist angle[23–28]. For twist angles  $\theta \lesssim 2^\circ$  the moiré electron bands are considerably narrower than the optical phonon energy ( $\sim 200$  meV), becoming as narrow as  $J \lesssim 10$ -20 meV near “magic” values of the twist angle  $\theta \sim 1^\circ$ . Such bandwidths are sufficient to eliminate the optical phonon emission, the main obstacle to observing coherent Bloch oscillations in wide bands.

The moiré graphene also clears other key requirements for observing Bloch oscillations. One is weak disorder scattering. Since the narrow bands are formed in a solid with a pristine near-perfect atomic order, they are less susceptible to disorder than the bands in synthetic MBE-grown semiconductor superlattices. This is manifested in a high carrier mobility and ballistic carrier transport observed over micron lengthscales at  $T = 0$ [27, 28]. Estimating the scattering time as  $\tau = l/v_F$  with the mean free path  $l \sim 1 \mu\text{m}$  and velocity  $v_F$  of about 1/30 of the graphene monolayer value  $10^6$  m/s gives  $\tau \sim 3 \cdot 10^{-11}$  s, a value comparable to that of graphene monolayer. The scattering rate can therefore be as low as  $\gamma_{\text{dis}} \sim 10^{-2} J$ .

Furthermore, the two-dimensional character of moiré graphene will help to suppress the instability due to inhomogeneous charge accumulation that drives the formation of electric field domains occurring in the stacks of quantum wells. Indeed, in the moiré setup the electric current is driven in the graphene plane in a manner that maintains the translation invariance of the system and does not cause local charging. In addition, gating is known to maintain a spatially uniform carrier density even under moderate to high currents.

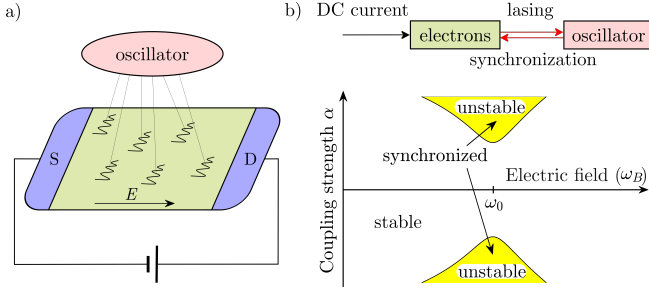


FIG. 1: a) Bloch-oscillating electrons synchronized by coupling to an oscillator mode. A DC electric field  $\mathbf{E}$  drives free-carrier oscillations with frequency  $\omega_B$  (wavy lines). The oscillations are at the same frequency for all carriers but are asynchronous (not in phase). Synchronized oscillations are achieved through coupling to an oscillator mode, depicted by the thin lines. b) A phase diagram showing the stable and unstable regimes, in which Bloch oscillations are asynchronous and synchronized, respectively. The carrier scattering rate  $\gamma$  is taken to be equal the oscillator damping rate  $\gamma_0$  (see Eq.(11)); phase diagrams for unequal  $\gamma$  and  $\gamma_0$  are pictured in Fig.4. The Bloch frequency  $\omega_B$  on the  $x$  axis is proportional to the electric field;  $\omega_0$  is the oscillator frequency, the coupling strength  $\alpha$  between each electron and the oscillator is defined in Eq.(9). Instability is easiest to achieve when  $\omega_B$  is tuned close to  $\omega_0$ . The flowchart on top shows the relationship between different degrees of freedom: the DC current drives free-carrier oscillations; being synchronized by the oscillator, they pump energy into the oscillator (the lasing effect).

Other appealing properties of moiré graphene are the lack of Zener transitions, suppressed by sizable minigaps separating the flat bands from the higher and lower minibands, and the weakness of the electron scattering by the long-wavelength acoustic phonons[29–31]. Added to that, the relatively large periodicity of moiré superlattices ( $a \sim 10\text{nm}$ ) reduces the required  $E$  field values:

$$\gamma = \max[\gamma_{\text{ph}}, \gamma_{\text{dis}}] < \omega_B < J/\hbar, \quad \omega_B = eEa/\hbar. \quad (1)$$

Using moderate  $E$  fields will help to avoid the Wannier-Stark ladder localization effects and charge instabilities.

Importantly, although all free carriers Bloch-oscillate with identical frequencies, these oscillations are *asynchronous*, as the oscillation phases are totally random and uncorrelated for different carriers. Therefore, in order to achieve collective continuous-wave Bloch oscillations driven by a direct current, the movement of different carrier must be synchronized. We outline a way to achieve this through coupling of the current-carrying channel to an oscillator mode in a THz resonator. The resonator frequency depends on system parameters, whereas the Bloch frequency is tunable by varying the applied electric field. As illustrated in Fig.1, this system develops an instability towards collective oscillations at a Bloch frequency when the latter is close to the oscillator frequency. In practice, the oscillator can be realized as a THz photonic or plasmonic resonator in a 2D or a 3D architecture[6, 32–36]. Phase-coherent oscillations achieved in this regime represent a realization of electrically pumped THz lasing.

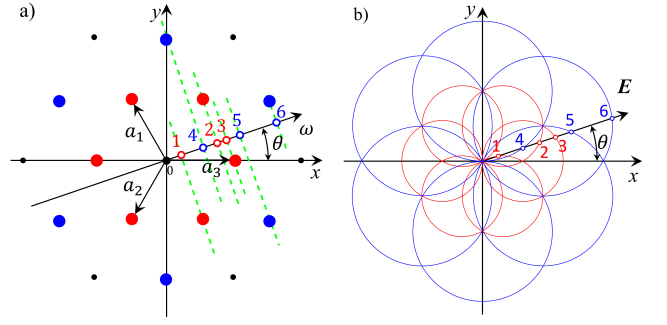


FIG. 2: a) Geometric construction of the frequency comb for Bloch oscillations, Eq.(2), at a generic electric field orientation relative to the superlattice. Frequencies  $\omega_l$  are found by projecting the real-space Bravais lattice points (solid circles) onto the 1D line parallel to  $\mathbf{E}$  (black arrow) as indicated by dashed green lines. The shortest and next-shortest vectors are shown as red and blue dots. Hollow circles, found by projection, give the frequencies in Eq.(2), where the emitted noise power  $P(\omega)$  peaks. b) Visualization of the comb  $\omega_l$  angle dependence vs.  $\mathbf{E}$  orientation relative to the superlattice.

Prior to tackling the synchronization problem we summarize the basic picture of the free-carrier Bloch oscillations in superlattices. The dynamics in superlattices of dimension  $D \geq 2$  differs from that in  $D = 1$  in that different carriers can move at different angles relative to the applied field[10, 19–22]. Despite this difference, the main properties of the one-dimensional Bloch oscillations persist. The Bloch frequencies remain discrete, taking values identical for all carriers in the system. The only new aspect is that different harmonics of the band dispersion produce oscillations with several different discrete frequency values. These frequencies are in general incommensurate with one another, forming a comb-like spectrum pictured in Figs.2 and 3.

The frequency comb dependence on the electric field orientation with respect to the superlattice is described by the geometric construction illustrated in Fig.2. Namely, possible frequencies are given by the projections of different Bravais lattice vectors  $\mathbf{a}_l = n_1 \mathbf{a}_1^{(0)} + n_2 \mathbf{a}_2^{(0)}$  on the applied field  $\mathbf{E}$ :

$$\omega_l = \frac{e}{\hbar} \mathbf{E} \cdot \mathbf{a}_l = \frac{e}{\hbar} E a_l \cos(\theta - \theta_l) \quad (2)$$

The dependence of the frequencies  $\omega_l$  on the field  $\mathbf{E}$  orientation and strength, as well as the tunability of moiré superlattices by the twist angle, provide knobs that will facilitate achieving Bloch oscillations in moiré graphene.

This result can be understood in very general terms by considering a tight binding bandstructure on a monoatomic lattice,

$$\epsilon(\mathbf{k}) = \sum_{l=1,2,\dots} -2J_l \cos(\mathbf{k} \cdot \mathbf{a}_l). \quad (3)$$

The Bravais lattice vectors  $\mathbf{a}_l$  describe hopping between different pairs of lattice sites, either nearest-neighbor or non-nearest-neighbor. Bloch-oscillating free carriers

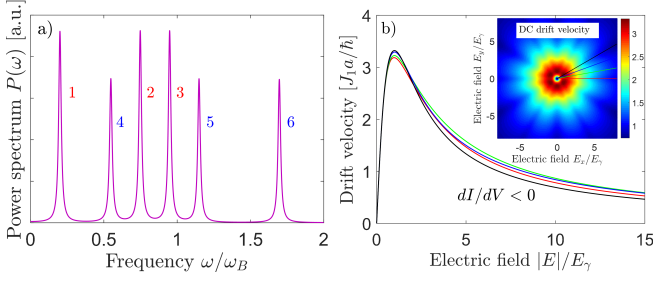


FIG. 3: a) The comb-like frequency spectrum of current fluctuations, Eqs.(5), consisting of finite-width resonances at the discrete frequency values  $\omega_l$ , Eq.(2); units:  $\omega_B = \frac{e}{\hbar} E a$ . The field orientation and labeling of different peaks match those in Fig.2. b) The direct-current drift velocity, Eq.(6). Shown is the full dependence (inset) and traces for several different field orientations. Bloch oscillations occur for field strength  $E > E_\gamma = \hbar\gamma/ea$ ; negative differential conductivity  $dI/dV < 0$  is a hallmark of this regime.

obey quasiclassical equations of motion

$$\hbar \frac{d\mathbf{k}}{dt} = e\mathbf{E}, \quad (4)$$

generating a linear time dependence  $\mathbf{k}(t) = \frac{e}{\hbar} \mathbf{E}t + \mathbf{k}_0$  with the linear part identical for all carriers and a carrier-specific initial value  $\mathbf{k}_0$ . With this bandstructure and an electric field of a generic orientation,  $\mathbf{E} = E(\cos\theta, \sin\theta)$ , the frequencies at which the time-dependent velocity of the electrons  $\mathbf{v}(t) = \frac{1}{\hbar} \nabla_{\mathbf{k}} \epsilon(\mathbf{k})|_{\mathbf{k}=\frac{e}{\hbar} \mathbf{E}t + \mathbf{k}_0}$  will oscillate are given by  $\mathbf{a}_l$  projected on  $\mathbf{E}$ , Eq.(2). The resulting dependence of the frequencies  $\omega_l$  on the orientation of  $\mathbf{E}$  is described by families of circles pictured in Fig.2.

Physically, discrete frequency values arise because electron trajectories sweep the (reduced) Brillouin zone (BZ) of a two-dimensional crystal in the direction set by the  $\mathbf{E}$  vector. Every time an electron reaches zone boundary it unklapps to the opposite side and continues forward, winding around the BZ at different frequencies in different crystal axes directions. At the same time, the average frequency along the direction of  $\mathbf{E}$  is the same for all carriers. This leads, for a general field orientation, to a quasiperiodic dynamics characterized by two fundamental frequencies which depend only on the field  $\mathbf{E}$  and lattice periodicity as described in Eq.(2), wherein  $\omega_l = n_1\omega_1 + n_2\omega_2$  in agreement with the geometric construction in Fig.2.

In the presence of momentum-relaxing scattering the frequency spectrum broadens into a sum of finite-width resonances centered at  $\omega = \omega_l$ . The quantity of interest is the autocorrelation function of current fluctuations  $P(\omega) = \frac{1}{2} \int_{-\infty}^{\infty} \langle \delta \mathbf{j}(t) \cdot \delta \mathbf{j}(t+\tau) \rangle e^{-i\omega\tau} d\tau$ . Simple analysis predicts a comb-like emitted power spectrum

$$P(\omega) = \sum_l \frac{P_l}{(\omega - \omega_l)^2 + \gamma^2} \quad (5)$$

(see Appendix). The Bloch oscillation regime corresponds to non-overlapping resonances. Since the frequen-

cies  $\omega_l$  are proportional to the applied field  $\mathbf{E}$  the oscillations appear when the field strength exceeds a threshold set by momentum-relaxing scattering,  $E_\gamma = \hbar\gamma/ea$ . At lower fields the resonances merge into a broadband noise spectrum, indicating a suppression of the oscillations.

In the Bloch oscillation regime the DC drift velocity exhibits negative differential conductivity  $dI/dV < 0$ , a characteristic behavior that provides a clear signature of this regime. A direct calculation (see Appendix) predicts

$$\mathbf{v}_{DC} = \sum_l \mathbf{a}_l \frac{2J_l f_l}{\hbar} \frac{\gamma \omega_l}{\gamma^2 + \omega_l^2}, \quad f_l = \sum_k f_0(k) e^{i\mathbf{a}_l \mathbf{k}}, \quad (6)$$

with  $f_0(k)$  the steady-state momentum distribution. The dependence on the field  $E$  is linear at small  $E < E_\gamma$  and falls off as  $1/E$  at large  $E > E_\gamma$ . Interestingly, current depends on the dimensionless quantity  $E/E_\gamma$  in a way that is independent of the specific value of  $\gamma$ . This behavior is illustrated in Fig.3(b). The drift velocity for electric fields in different directions is shown in the inset.

Next, we turn to the discussion of Bloch oscillations synchronized by coupling to an oscillator mode:

$$H = \sum_i [\epsilon(\mathbf{p}_i) - e\mathbf{E}\mathbf{x}_i - \alpha Q x_i] + \frac{1}{2m} P^2 + \frac{\omega_0^2 m}{2} Q^2. \quad (7)$$

Here  $\epsilon(\mathbf{p})$  is the band dispersion,  $\mathbf{p}_i$  and  $\mathbf{x}_i$  are the momenta and coordinates of the electrons;  $P$  and  $Q$  are the momentum and amplitude of the oscillator. The Bloch electron coupling to the oscillator and the external field is through potentials  $U(\mathbf{x}_i) = -e\mathbf{E}\mathbf{x}_i - \alpha Q x_i$  seen by each of the electrons. In this approach we ignore the direct carrier-carrier interactions, treating electron dynamics in a free-particle approximation. Bloch oscillations are driven by the electric field  $E$ , the term  $-\alpha Q x_i$  describes coupling of the electrons to the oscillator mode. In practice the oscillator can be realized as e.g. THz photonic or plasmonic resonators[6, 32–36].

We consider the equations of motion originating from the Hamiltonian above. We wish to integrate out the carrier degrees of freedom and derive a closed-form dynamics for the oscillator. For that purpose we solve equations of motion for the  $i$ -th electron beginning from the time  $t'_i < t$  when its state was last reset by scattering and the Hamiltonian dynamics described by Eq.(7) had started.

The full set of equations of motion for the electrons and the oscillator is

$$\begin{aligned} \dot{\mathbf{p}}_i &= -\frac{\partial H}{\partial \mathbf{x}_i} = e\mathbf{E} + \alpha Q(t), & \dot{\mathbf{x}}_i &= \frac{\partial H}{\partial \mathbf{p}_i} = \frac{\partial \epsilon(\mathbf{p}_i)}{\partial \mathbf{p}_i} \\ \dot{P} &= -m\omega_0^2 Q + \sum_i \alpha x_i, & \dot{Q} &= P/m. \end{aligned} \quad (8)$$

Eliminating  $P(t)$  yields a second-order equation of motion for the oscillator mode  $Q(t)$ , driven by an external force given by a sum of contributions due to the electrons

$$\ddot{Q}(t) + \omega_0^2 Q(t) = f(t), \quad f(t) = \frac{\alpha}{m} \sum_i x_i(t). \quad (9)$$

Importantly, the cumulative effect due to the electrons, given by the quantity  $f(t)$ , gives rise to a “memory effect” in the oscillator dynamics. Each term in the sum  $\sum_i x_i(t)$  is given by a solution of the equations of motion for  $x_i(t)$  and  $p_i(t)$ , Eq.(8), initialized at an earlier random time  $t'_i < t$ . The oscillator dynamics  $Q(t)$ ,  $P(t)$  during the time intervals  $t'_i < \tau < t$  affects the electron states  $x_i(t)$ ,  $p_i(t)$ , giving rise to a back-action  $f(t) = \frac{\alpha}{m} \sum_i x_i(t)$  with the dynamical memory originating from the dependence on  $Q(\tau)$  and  $P(\tau)$  at the earlier times  $\tau < t$ .

The feedback due to this memory effect enables synchronization of Bloch dynamics, resulting in a macroscopic oscillating current generated by Bloch-oscillating electrons. To describe the instability we compute the backaction term linearized in  $Q(t')$  (the analysis is lengthy but straightforward, see Appendix). Substituting the result in Eq.(9) gives a characteristic equation for  $\omega$  of the form

$$\omega_0^2 - \omega^2 = \frac{i\lambda}{\omega} \left( \frac{2\gamma^2}{(\gamma^2 + \omega_B^2)(\gamma - i\omega)} + \frac{\gamma}{(\omega + i\gamma)^2 - \omega_B^2} \right), \quad (10)$$

where we defined  $\lambda = N \frac{\alpha^2 a v_0}{m \hbar}$  with  $N$  the total number of Bloch-oscillating electrons.

The system becomes unstable when Eq.(10) admits solutions in the upper halfplane of complex  $\omega$ . Before exploring this instability we inspect, as a sanity check, the regime of highly damped Bloch oscillations,  $\gamma \gg \omega_B, \omega_0$ . In this case, Eq.(10) reads  $\omega_0^2 - \omega^2 = \frac{i\lambda}{\omega\gamma}$ . At large  $\gamma$ , the roots of this equation are close to  $\pm\omega_0$ . Writing  $\omega = \pm\omega_0 + \Delta\omega$ , at leading order in  $1/\gamma$  we find  $\Delta\omega = -i\frac{i\lambda}{\omega_0^2\gamma}$ . Negative imaginary part indicates that no instability arises in this regime, i.e. the driven system is stabilized by high damping.

Next, we consider a weak damping  $\gamma \ll \omega_B, \omega_0$ . The behavior in this case is simplest to understand close to the resonance between the oscillator and Bloch frequencies,  $\omega_0 \approx \omega_B$ . Focusing on the frequencies  $\omega$  near the resonance, where the last term in Eq.(10) dominates, we ignore the first non-resonant term and obtain

$$(\omega_0^2 - (\omega + i\gamma_0)^2)((\omega + i\gamma)^2 - \omega_B^2) = \frac{i\lambda\gamma}{\omega}. \quad (11)$$

Here we added the damping rate  $\gamma_0$  for the oscillator. Working near the resonance and expanding in a small  $\delta\omega = \omega - \omega_0 \ll \omega_0 \approx \omega_B$  to obtain the complex frequency roots positioned near  $\omega_0$ , the characteristic equation becomes

$$(\omega - \omega_0 + i\gamma_0)(\omega + i\gamma - \omega_B) = -i\eta/4, \quad \eta = \frac{\lambda\gamma}{\omega_0^3}. \quad (12)$$

The properties of Eq.(12) are simplest to understand when  $\gamma_0 = \gamma$ . In this case, the roots are

$$\omega_{1,2} = -i\gamma + \frac{\omega_B + \omega_0 \pm \sqrt{(\omega_B - \omega_0)^2 - i\eta}}{2} \quad (13)$$

The system is stable if  $\text{Im } \omega_{1,2} < 0$  and unstable otherwise. Using the identity

$$\text{Im} \left( \sqrt{x - i\eta} \right) = -\text{sgn } \eta \sqrt{\frac{\sqrt{x^2 + \eta^2} - x}{2}} \quad (14)$$

with  $x = (\omega_B - \omega_0)^2$ , we can write the condition for the instability as

$$\eta^2 > \left( (\omega_B - \omega_0)^2 + 4\gamma^2 \right) 16\gamma^2. \quad (15)$$

This criterion predicts the Bloch frequency  $\omega_B$  and the coupling strength  $\lambda$  values for which an instability towards a synchronized dynamics may occur, giving the phase diagram pictured in Fig.1. As one might expect on general grounds, the instability is easiest to achieve when Bloch oscillations are in resonance with the oscillator,  $\omega_B = \omega_0$ . Tuning away from the resonance suppresses the instability. The instability signals the onset of a collective regime in which Bloch-oscillating electrons become synchronized through coupling to the oscillator mode.

In summary, the unique electronic properties of the flat bands in moiré graphene, such as the bandwidth considerably narrower than the optical phonon energy, the  $\sim 10\text{nm}$ -large superlattice periodicity and relatively high mobility, will facilitate observing the Bloch oscillations. The two-dimensional nature of the system offers additional benefits: the carriers, which are fully exposed, can be coupled to a nearby oscillator mode that will synchronize their movements to enable phase-coherent collective oscillations, a regime in which current-pumped THz lasing can be realized and explored.

This work was supported by the Science and Technology Center for Integrated Quantum Materials, NSF Grant No. DMR-1231319; and Army Research Office Grant W911NF-18-1-0116 (L.L.). E.K. acknowledges financial support by the Research Travel Grant of the Karlsruhe House of Young Scientists (KHYS)

- 
- [1] N. W. Ashcroft and N. D. Mermin, Solid State Physics (Saunders, Philadelphia, 1976).  
 [2] A. B. Pippard, The Dynamics of Conduction Electrons

- (Gordon and Breach Science Publishers, Inc., New York, 1965).  
 [3] L. Esaki and R. Tsu, Superlattice and Negative Differen-

- tial Conductivity in Semiconductors, IBM J. Res. Dev., **14**, 61-65 (1970).
- [4] S. A. Kitorov, G. S. Simin, and V. Y. Sindalovskii, Bragg reflections and the high-frequency conductivity of an electronic solid-state plasma, *Fizika Tverdogo Tela*, **13**, 2230-2233 (1971) [*Soviet Physics - Solid State* **13**, 1872-1874 (1972)]
  - [5] H. Kroemer, On the nature of the negative-conductivity resonance in a superlattice Bloch oscillator, arXiv:cond-mat/0007482 (2000).
  - [6] P. G. Savvidis, B. Kolasa, G. Lee, and S. J. Allen, Resonant Crossover of Terahertz Loss to the Gain of a Bloch oscillating InAs/AlSb Superlattice, *Phys. Rev. Lett.* **92**, 196802 (2004).
  - [7] A. Sibille, J. F. Palmier, H. Wang, and F. Molloy, Observation of Esaki-Tsu negative differential velocity in GaAs/AlAs superlattices, *Phys. Rev. Lett.* **64**, 52 (1990).
  - [8] J. Feldmann, K. Leo, J. Shah, D. A. B. Miller, and J. E. Cunningham, T. Meier, G. von Plessen, A. Schulze, P. Thomas, and S. Schmitt-Rink, Optical investigation of Bloch oscillations in a semiconductor superlattice, *Phys. Rev. B* **46**, 7252 (1992).
  - [9] C. Waschke, H. G. Roskos, R. Schwedler, K. Leo, H. Kurz, and K. Kohler, Coherent submillimeter-wave emission from Bloch oscillations in a semiconductor superlattice, *Phys. Rev. Lett.* **70**, 3319 (1993).
  - [10] A. Rauh and G. H. Wannier, Theory of stark ladders in the optical absorption of solids, *Solid State Commun.* **15**, 1239 (1974).
  - [11] T. Hyart, K. N. Alekseev, and E. V. Thuneberg, Bloch gain in dc-ac-driven semiconductor superlattices in the absence of electric domains, *Phys. Rev. B* **77**, 165330 (2008).
  - [12] T. Hyart, N. V. Alexeeva, J. Mattas, and K. N. Alekseev, Terahertz Bloch Oscillator with a Modulated Bias, *Phys. Rev. Lett.* **102**, 140405 (2009).
  - [13] T. Hyart, J. Mattas, and K. N. Alekseev, Model of the Influence of an External Magnetic Field on the Gain of Terahertz Radiation from Semiconductor Superlattices, *Phys. Rev. Lett.* **103**, 117401 (2009).
  - [14] M. Ben Dahan, E. Peik, J. Reichel, Y. Castin, and C. Salomon, Bloch Oscillations of Atoms in an Optical Potential, *Phys. Rev. Lett.* **76**, 4508 (1996).
  - [15] B. P. Anderson, M. A. Kasevich, Macroscopic Quantum Interference from Atomic Tunnel Arrays, *Science* **282** (5394), 1686-1689 (1998).
  - [16] O. Morsch, J. H. Muller, M. Cristiani, D. Ciampini, and E. Arimondo, Bloch Oscillations and Mean-Field Effects of Bose-Einstein Condensates in 1D Optical Lattices, *Phys. Rev. Lett.* **87**, 140402 (2001).
  - [17] M. Cristiani, O. Morsch, J. H. Muller, D. Ciampini, and E. Arimondo, Experimental properties of Bose-Einstein condensates in one-dimensional optical lattices: Bloch oscillations, Landau-Zener tunneling, and mean-field effects, *Phys. Rev. A* **65**, 063612 (2002).
  - [18] H. Ott, E. de Mirandes, F. Ferlaino, G. Roati, G. Modugno, and M. Inguscio, Collisionally Induced Transport in Periodic Potentials, *Phys. Rev. Lett.* **92**, 160601 (2004).
  - [19] M. Gluck, F. Keck, A. R. Kolovsky, and H. J. Korsch, Wannier-Stark resonances in optical and semiconductor superlattices, *Phys. Reps.* **366** (3), 103-182 (2002).
  - [20] I. A. Dmitriev and R. A. Suris *Semiconductors* **35**, 212 (2001).
  - [21] I. A. Dmitriev and R. A. Suris *Semiconductors* **36**, 1364 (2002).
  - [22] A. R. Kolovsky, E. N. Bulgakov, Wannier-Stark states and Bloch oscillations in the honeycomb lattice, *Phys. Rev. A* **87** (3), 033602 (2013).
  - [23] R. Bistritzer and A. H. MacDonald, Moiré bands in twisted double-layer graphene. *Proc. Nat. Acad. Sci.* **108**, 12233-12237 (2011).
  - [24] Y. Cao, V. Fatemi, A. Demir, S. Fang, S. L. Tomarken, J. Y. Luo, J. D. Sanchez-Yamagishi, K. Watanabe, T. Taniguchi, E. Kaxiras, R. C. Ashoori, and P. Jarillo-Herrero, Correlated insulator behaviour at half-filling in magic-angle graphene superlattices. *Nature* **556**, 80-84 (2018).
  - [25] Y. Cao, V. Fatemi, S. Fang, K. Watanabe, T. Taniguchi, E. Kaxiras, and P. Jarillo-Herrero, Unconventional superconductivity in magic-angle graphene superlattices. *Nature* **556**, 43-50 (2018).
  - [26] Y. Cao, J. Y. Luo, V. Fatemi, S. Fang, J. D. Sanchez-Yamagishi, K. Watanabe, T. Taniguchi, E. Kaxiras, and P. Jarillo-Herrero, Superlattice-Induced Insulating States and Valley-Protected Orbits in Twisted Bilayer Graphene. *Phys. Rev. Lett.* **117**, 116804 (2016).
  - [27] Y. Kim, P. Herlinger, P. Moon, M. Koshino, T. Taniguchi, K. Watanabe and J. H. Smet, Charge Inversion and Topological Phase Transition at a Twist Angle Induced van Hove Singularity of Bilayer Graphene, *Nano Lett.* **16**, 5053-5059 (2016).
  - [28] A. I. Berdyugin, B. Tsim, P. Kumaravadivel, S. G. Xu, A. Ceferino, A. Knothe, R. Krishna Kumar, T. Taniguchi, K. Watanabe, A. K. Geim, I. V. Grigorieva, V. I. Fal'ko, Minibands in twisted bilayer graphene probed by magnetic focusing, *Sci. Adv.* **6**: eaay7838 (2020)
  - [29] R. Bistritzer and A. H. MacDonald, Electronic cooling in graphene, *Phys. Rev. Lett.*, **102**, 206410 (2009).
  - [30] W. K. Tse, S. Das Sarma, Energy relaxation of hot Dirac fermions in graphene. *Phys. Rev. B*, **79**, 235406 (2009).
  - [31] J. C. W. Song, M. Y. Reizer, L. S. Levitov, Disorder-assisted electron-phonon scattering and cooling pathways in graphene. *Phys. Rev. Lett.* **109**, 106602 (2012).
  - [32] L. Ju, et al. Graphene plasmonics for tunable terahertz metamaterials. *Nat. Nanotechnol.* **6**, 630-643 (2011).
  - [33] H. Yan, et al. Tunable infrared plasmonic devices using graphene/insulator stacks. *Nat. Nanotechnol.* **7**, 330-334 (2012).
  - [34] H. Yan, et al. Infrared spectroscopy of tunable dirac terahertz magneto-plasmons in graphene. *Nano. Lett.* **12**, 3766-3771 (2012).
  - [35] N. H. Tu, K. Yoshioka, S. Sasaki, M. Takamura, K. Muraki and N. Kumada, Active spatial control of terahertz plasmons in graphene, *Communications Materials* volume 1, Article number: 7 (2020)
  - [36] L. Ateshian, H. Choi, M. Heuck, and D. Englund, Terahertz Light Sources by Electronic-Oscillator-Driven Second Harmonic Generation in Extreme-Confinement Cavities, arXiv:2009.13029
  - [37] Sh. M. Kogan and A. Ya. Shulman, Extraneous random forces and equations for correlation functions in the theory of nonequilibrium fluctuations, *Fiz. Tverd. Tela (Leningrad)* **12**(4), 1119-1123 (1970) [*Sov. Phys. - Solid State* **12**(4), 874 (1970)].
  - [38] Sh. Kogan, *Electronic Noise and Fluctuations in Solids* (Cambridge University Press, 2008)

## I. APPENDIX

Here we provide the details of the analysis of the back-action on the oscillator due to Bloch-oscillating carriers. We work with the equations of motion as given in Eqs.(8). We average over the randomness in the starting times  $t'_i$  ignoring the associated noise. This simple approach will be sufficient to understand the synchronization effect. The role of randomness and noise will be discussed elsewhere.

As a first step, we integrate Bloch dynamics of the  $i$ -th electron for times  $t'_i < \tau < t$ , which gives

$$\mathbf{p}_i(t) = e\mathbf{E}(t - t'_i) + \mathbf{p}_i(t'_i) + \alpha \int_{t'_i}^t Q(\tau') d\tau' \quad (\text{I.1})$$

$$\mathbf{x}_i(t) = \mathbf{x}_i(t'_i) + \int_{t'_i}^t \mathbf{v}_i(\tau) d\tau,$$

where  $\mathbf{v}_i(\tau) = \sum_l \frac{2J_l \mathbf{a}_l}{\hbar} \sin[\mathbf{a}_l \cdot \mathbf{p}(t)/\hbar]$ . Averaging over the starting times  $t'_i$  must be carried out using the survival probability obeying the Poisson statistics  $dp = dt\gamma e^{-\gamma(t-t'_i)}$ .

It is instructive to first apply these relations to the free-carrier dynamics in the absence of coupling to the oscillator,  $\alpha = 0$ . In this case different carriers are totally decoupled and thus not synchronized. The drift velocity can be found by averaging  $\mathbf{v}_i(t)$  as

$$\begin{aligned} \langle \mathbf{v}_i(t) \rangle &= \sum_{\mathbf{k}'} \int_{-\infty}^t dt' \gamma e^{-\gamma(t-t')} \mathbf{v}_i(t, t') \\ &= \sum_{\mathbf{k}'} \sum_l \frac{J_l \mathbf{a}_l}{i\hbar} \gamma \left[ \frac{e^{i\mathbf{a}_l \cdot \mathbf{k}'}}{\gamma - i\frac{e}{\hbar} \mathbf{a}_l \cdot \mathbf{E}} - \frac{e^{-i\mathbf{a}_l \cdot \mathbf{k}'}}{\gamma + i\frac{e}{\hbar} \mathbf{a}_l \cdot \mathbf{E}} \right], \quad (\text{I.2}) \end{aligned}$$

where  $\sum_{\mathbf{k}'}$  is a shorthand notation for averaging over the initial momentum distribution  $\int \frac{d^2k}{(2\pi)^2} f_0(\mathbf{k}')$  (here assumed to be steady-state). The quantity  $\mathbf{v}_i(t, t')$  under the integral over  $t'$  is a sum of harmonics with frequencies  $\omega_l$ , arising from the carrier velocity time dependence

$$\mathbf{v}_i(t, t') = \sum_l \frac{2J_l \mathbf{a}_l}{\hbar} \sin \left[ \mathbf{a}_l \cdot \left( \frac{e}{\hbar} \mathbf{E}(t - t') + \mathbf{k}' \right) \right]. \quad (\text{I.3})$$

Simplifying the result in Eq.I.2 yields the drift velocity

$$\mathbf{v}_{\text{DC}} = \sum_{\mathbf{k}'} \sum_l \frac{2J_l \mathbf{a}_l}{\hbar} \cos(\mathbf{a}_l \cdot \mathbf{k}') \frac{\gamma \frac{e}{\hbar} \mathbf{a}_l \cdot \mathbf{E}}{\gamma^2 + (\frac{e}{\hbar} \mathbf{a}_l \cdot \mathbf{E})^2}. \quad (\text{I.4})$$

Given by a sum of the terms  $\frac{\gamma \omega_l}{\gamma^2 + \omega_l^2}$ , the dependence  $v_{\text{DC}}$  vs.  $E$  is nonmonotonic, growing linearly at  $E \lesssim E_\gamma = \gamma\hbar/ea$  and decreasing at  $E \gtrsim E_\gamma$ ; at weak fields it matches the Drude theory prediction. The negative differential conductivity  $dI/dV < 0$  is a testable signature of the Bloch-oscillation regime.

The spectrum of current fluctuations, Eq.(5), can be obtained in a similar manner. The velocity time dependence  $\mathbf{v}_i(t, t')$  is a sum of harmonics with frequencies  $\omega = \omega_l$ ; each harmonic producing a resonance broadened by the damping rate  $\gamma$ . Indeed, evaluating the Fourier components and averaging over the initial times gives

$$\int_{-\infty}^t dt' \gamma e^{-\gamma(t-t')} \mathbf{v}_i(t, t') e^{-i\omega(t-t')} \quad (\text{I.5})$$

$$= \sum_l \frac{J_l \mathbf{a}_l}{i\hbar} \gamma \left[ \frac{e^{i\mathbf{a}_l \cdot \mathbf{k}'}}{\gamma - i(\omega + \omega_l)} - \frac{e^{-i\mathbf{a}_l \cdot \mathbf{k}'}}{\gamma - i(\omega - \omega_l)} \right]. \quad (\text{I.6})$$

Taking squares of the absolute values yields a fairly cumbersome expression for the noise spectrum. In the small- $\gamma$  limit, achieved at  $E \gtrsim E_\gamma$ , it represents a comb of sharp Lorentzians plus a background part, see Eq.(5) and Fig.3.

Next, we reinstate the coupling to the oscillator and proceed with the analysis of synchronization. For conciseness, we focus on a resonance approximation valid near one of the resonances  $\omega = \omega_l$  in Eq.(5), at  $\omega_B \gg \gamma$ . In what follows, without loss of generality, we take  $\mathbf{E}$  to be parallel to  $\mathbf{a}_l$ , and denote  $\omega_l$  and  $\mathbf{a}_l$  as  $\omega_B$  and  $a$ , respectively. Generalizing to the large- $\gamma$  case and other field orientations will be straightforward. The special cases of field orientation such that  $\mathbf{E} \cdot \mathbf{a}_l \approx \mathbf{E} \cdot \mathbf{a}_{l'}$ , when two resonances can be excited simultaneously, will be discussed elsewhere.

The back-action of the carriers on the oscillator, given by the sum of carrier displacements  $f(t) = \frac{\alpha}{m} \sum_i x_i(t)$  in Eq.9 averaged over the starting times  $t'_i$  with the Poissonian survival probability  $dp = dt\gamma e^{-\gamma(t-t'_i)}$ , equals

$$\begin{aligned} \langle x_i(t) \rangle &= \langle x_i(t') \rangle + \int_{-\infty}^t dt' \gamma e^{-\gamma(t-t')} \int_{t'}^t d\tau v_0 \sin \frac{ap_i(\tau)}{\hbar} \\ &= \int_{-\infty}^t dt' \gamma e^{-\gamma(t-t')} \int_{t'}^t d\tau v_0 \sin(\phi(\tau)), \quad v_0 = \frac{2aJ_l}{\hbar}, \quad (\text{I.7}) \end{aligned}$$

where we denote  $\phi(\tau) = \omega_B(\tau - t') + \frac{\alpha a}{\hbar} \int_{t'}^\tau Q(\tau') d\tau'$ . In what follows we drop the starting displacement term  $\langle x_i(t') \rangle$ , assuming that it vanishes under averaging as expected for a spatially uniform distribution.

The single mode dynamics is now described by Eq.(9) with the right-hand side replaced with a back-action memory function  $\frac{\alpha}{m} N \langle x_i(t) \rangle$ , where  $N$  is the number of Bloch electrons. We will consider the dynamics at lowest nonvanishing order in  $Q(t)$ , assuming the latter to be small. First, setting  $Q(\tau') = 0$  and integrating over  $\tau$ , we find  $\langle x_i^{(0)}(t) \rangle = \frac{v_0 \omega_B}{\gamma^2 + \omega_B^2}$ , a constant displacement that gives a time independent contribution to  $f(t)$  in Eq.(9), which can be compensated for by shifting the oscillator equilibrium. Next, at first order in  $Q(t)$ , we Taylor-expand the sine term to obtain

$$\langle x_i^{(1)}(t) \rangle = \int_{-\infty}^t dt' \gamma e^{-\gamma(t-t')} \left( \int_{t'}^t d\tau v_0 \cos(\omega_B(\tau - t')) \left[ \frac{\alpha a}{\hbar} \int_{t'}^{\tau} Q(\tau') d\tau' \right] \right). \quad (\text{I.8})$$

Plugging in a harmonic dependence  $Q(t) = Q_0 e^{-i\omega t}$ , we evaluate the integrals over  $\tau'$  and  $\tau$  as

$$\begin{aligned} \int_{t'}^t d\tau v_0 \cos(\omega_B(\tau - t')) \left[ \frac{\alpha a}{\hbar} \int_{t'}^{\tau} Q(\tau') d\tau' \right] &= \int_{t'}^t d\tau v_0 \cos(\omega_B(\tau - t')) \left[ \frac{i\alpha a}{\hbar\omega} Q_0 (e^{-i\omega\tau} - e^{-i\omega t'}) \right] \\ &= \frac{i\alpha a v_0}{\hbar\omega} Q_0 \left( e^{-i\omega t} \frac{e^{i\omega_B(t-t')} - e^{i\omega(t-t')}}{i(\omega_B - \omega)} + e^{-i\omega t'} \frac{e^{-i\omega_B(t-t')} - e^{i\omega(t-t')}}{-i(\omega_B + \omega)} - e^{-i\omega t'} \frac{\sin \omega_B(t-t')}{\omega_B} \right). \end{aligned} \quad (\text{I.9})$$

Integration over  $t' < t$  in Eq.(I.8) can now be carried out with the help of the identity

$$\int_{-\infty}^t dt' \gamma e^{-\gamma(t-t')} e^{-i\Omega(t-t')} = \frac{\gamma}{\gamma + i\Omega},$$

giving

$$\begin{aligned} \langle x_i^{(1)}(t) \rangle &= \frac{i\alpha a v_0}{\hbar\omega} Q_0 e^{-i\omega t} \left( \frac{\frac{\gamma}{\gamma - i\omega_B} - \frac{\gamma}{\gamma - i\omega}}{i(\omega_B - \omega)} + \frac{\frac{\gamma}{\gamma + i\omega_B} - \frac{\gamma}{\gamma - i\omega}}{-i(\omega_B + \omega)} - \frac{\frac{\gamma}{\gamma - i(\omega + \omega_B)} - \frac{\gamma}{\gamma - i(\omega - \omega_B)}}{2i\omega_B} \right) \\ &= \frac{i\alpha a v_0}{\hbar\omega} Q_0 e^{-i\omega t} \left( \frac{\gamma}{(\gamma - i\omega_B)(\gamma - i\omega)} + \frac{\gamma}{(\gamma + i\omega_B)(\gamma - i\omega)} - \frac{\gamma}{(\gamma - i(\omega + \omega_B))(\gamma - i(\omega - \omega_B))} \right) \\ &= \frac{i\alpha a v_0}{\hbar\omega} Q_0 e^{-i\omega t} \left( \frac{2\gamma^2}{(\gamma^2 + \omega_B^2)(\gamma - i\omega)} + \frac{\gamma}{(\omega + i\gamma)^2 - \omega_B^2} \right). \end{aligned} \quad (\text{I.10})$$

Substituting this result in Eq.(9) gives a characteristic equation for  $\omega$  of the form given in Eq.(10). The instability criterion and the phase diagram for the oscillator damping equal to that of Bloch-oscillating carriers is discussed in the main text (see Fig.1 and accompanying discussion).

It is instructive to extend this analysis to the more general case of unequal damping rates for the oscillator and electrons,  $\gamma_0 \neq \gamma$ . After some algebra we arrive at the instability criterion

$$\begin{aligned} (\eta + 2(\gamma - \gamma_0)(\omega_B - \omega_0))^2 &> \left( (\omega_B - \omega_0)^2 + 4\gamma\gamma_0 \right) \\ &\times 4(\gamma + \gamma_0)^2. \end{aligned} \quad (\text{I.11})$$

A new interesting behavior found for  $\gamma_0 \neq \gamma$  is an asymmetry between  $\omega_B$  blue-shifted and red-shifted away from  $\omega_0$ , with the instability threshold lower for  $\omega_B > \omega_0$  and higher for  $\omega_B < \omega_0$  when  $\gamma_0 < \gamma$ , and vice versa when  $\gamma_0 > \gamma$ , as illustrated in Fig. 4. The asymmetry is particularly striking in the limit  $\gamma_0/\gamma \rightarrow 0$ : for  $\omega_B > \omega_0$  the instability occurs at the coupling values  $\eta$  much smaller than those in Eq.(15), whereas for  $\omega_B < \omega_0$  the instability threshold remains on the same order as in Eq.(15). Furthermore, perhaps somewhat counterintuitively, for

$\gamma_0/\gamma \rightarrow 0$  the lowest value of coupling at which the instability sets in occurs far away from the resonance  $\omega_B = \omega_0$ .

The origin of this asymmetry is closely related to the mechanism that enables the synchronized behavior. When the oscillator is undamped, synchronization arises due to the electrons pumping energy into the oscillator mode; subsequently, when this energy is passed back to electrons, they become synchronized with the oscillator, and with each other. However, at a weak coupling  $\eta$ , the energy transfer from the Bloch-oscillating electrons into the oscillator is possible only if  $\hbar\omega_B > \hbar\omega_0$ , indicating that the instability is easier to reach for  $\omega_B$  values blue-shifted from  $\omega_0$ .

The above argument also suggests a reversal in the asymmetry when Bloch oscillations are weakly damped compared to the oscillator damping,  $\gamma \ll \gamma_0$ . Indeed, in this case it is the electron subsystem that serves as the main reservoir for energy storage, whereas the role of the oscillator mode is merely to lock the phases of different Bloch-oscillating carriers. Pumping energy into the collective mode now requires  $\hbar\omega_B < \hbar\omega_0$ . We therefore expect that in this limit the instability will occur at lower  $\eta$  values for  $\omega_B$  red-shifted from  $\omega_0$ . This is exactly what Eq.(I.11) predicts (see Fig.4).

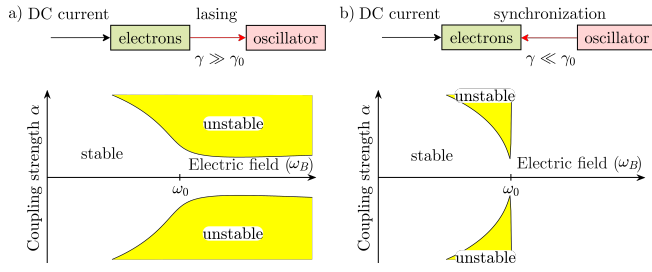


FIG. 4: The lasing and synchronization regimes. a) Lasing ( $\gamma \gg \gamma_0$ ). In this case, the oscillator is under-damped and serves as the main reservoir of the energy. Energy of the electrons is more easily pumped to the oscillator when  $\omega_B > \omega_0$ . Shown is the phase diagram for  $\gamma = 100\gamma_0$ . b) Synchronization ( $\gamma \ll \gamma_0$ ). In this case, the oscillator is over-damped and the electrons serve as the main reservoir of the energy. Energy of the oscillator is more easily pumped to the electrons when  $\omega_B < \omega_0$ . Shown is the phase diagram for  $100\gamma = \gamma_0$ . The instability criterion is a sign change of the imaginary parts of the roots of Eq. (11), which is negative in the stable regime and becomes positive in the unstable regime.